Journal Pre-proof

[Fe(CN)$_6$] Vacancy-boosting Oxygen Evolution Activity of Co-based Prussian Blue Analogues for Hybrid Sodium-air Battery

Yao Kang, Shuo Wang, Kwan San Hui, Hai-Feng Li, Feng Liang, Xin-Lin Wu, Qiuju Zhang, Wei Zhou, Liang Chen, Fuming Chen, Kwun Nam Hui

Please cite this article as: Y. Kang, S. Wang, K. San Hui, H.-F. Li, F. Liang, X.-L. Wu, Q. Zhang, W. Zhou, L. Chen, F. Chen, K.N. Hui, [Fe(CN)$_6$] Vacancy-boosting Oxygen Evolution Activity of Co-based Prussian Blue Analogues for Hybrid Sodium-air Battery, *Materials Today Energy*, https://doi.org/10.1016/j.mtener.2020.100572.

This is a PDF file of an article that has undergone enhancements after acceptance, such as the addition of a cover page and metadata, and formatting for readability, but it is not yet the definitive version of record. This version will undergo additional copyediting, typesetting and review before it is published in its final form, but we are providing this version to give early visibility of the article. Please note that, during the production process, errors may be discovered which could affect the content, and all legal disclaimers that apply to the journal pertain.

Credit Author statement

**Yao Kang**: Investigation, Conceptualization, Methodology, Writing-Original Draft. **Shuo Wang**: Software, Validation. **Kwan San Hui**: Validation, Writing-review & editing, Funding acquisition. **Hai-feng Li**: Software. **Feng Liang**: Writing Reviewing & Editing. **Xi-Lin Wu**: Writing Reviewing & Editing. **Qiuju Zhang**: Writing-review & Editing. **Wei Zhou**: Data curation. **Fuming Chen**: Funding acquisition, Writing-review & editing. **Kwun Nam Hui**: Supervision, Funding acquisition, Writing-Reviewing and Editing.
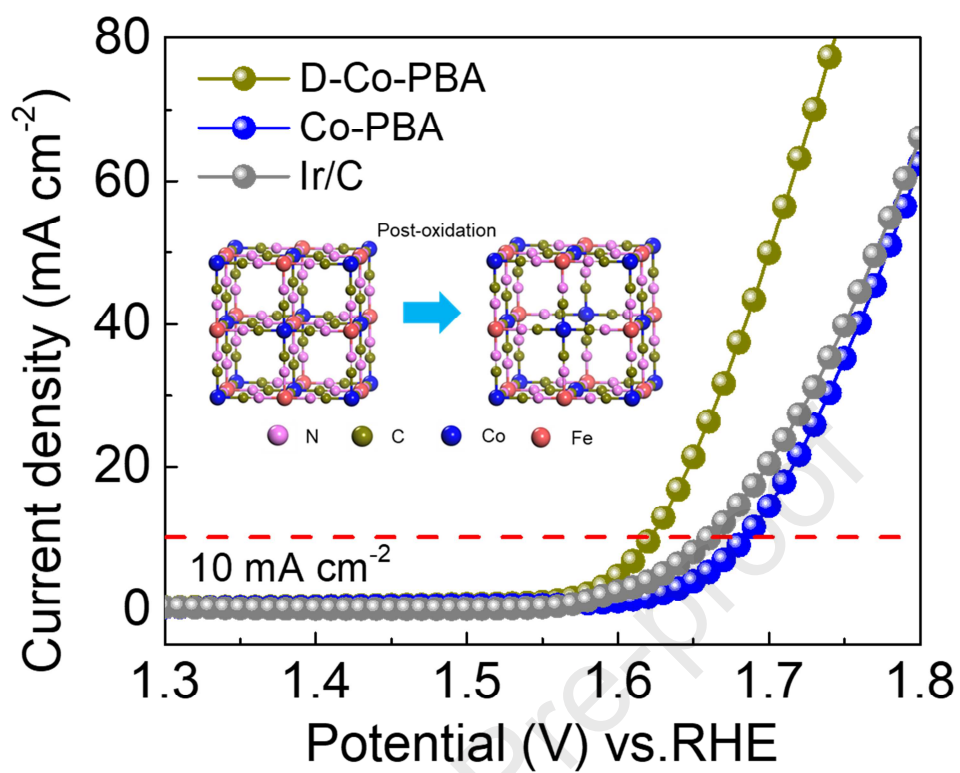
1   **[Fe(CN)₆] Vacancy-boosting Oxygen Evolution Activity of Co-based Prussian**

2   **Blue Analogues for Hybrid Sodium-air Battery**

3   Yao Kang [a, #], Shuo Wang [a, #], Kwan San Hui [b, *], Hai-Feng Li[a], Feng Liang[c], Xin-Lin Wu[d],

4   Qiuju Zhang[e], Wei Zhou[f], Liang Chen [e, **], Fuming Chen[g, ****], Kwun Nam Hui [a, *****]

5   [a] Joint Key Laboratory of the Ministry of Education, Institute of Applied Physics and

6   Materials Engineering, University of Macau, Avenida da Universidade, Taipa, Macau SAR

7   999078, China.

8   [b] Engineering, Faculty of Science, University of East Anglia, Norwich, NR4 7TJ, United

9   Kingdom.

10   [c] State Key Laboratory of Complex Nonferrous Metal Resources Clean Utilization, Kunming

11   University of Science and Technology, Kunming 650093, China.

12   [d] College of Geography and Environmental Science, Zhejiang Normal University, Jinhua

13   321004, China.

14   [e] Ningbo Institute of Materials Technology and Engineering, Chinese Academy of Sciences,

15   Ningbo, Zhejiang 315201, China.

16   [f] Department of Mechanical & Electrical Engineering, Xiamen University, Xiamen 361005,

17   China.

18   [g] Guangdong Provincial Key Laboratory of Quantum Engineering and Quantum Materials,

19   School of Physics and Telecommunication Engineering, South China Normal University,

20   Guangzhou 510006, China.

21   # These authors contribute equally

22   * Corresponding author

23   Kwan San Hui, E-mail: k.hui@uea.ac.uk

24   Liang Chen, E-mail: chenliang@nimte.ac.cn

25   Fuming Chen, E-mail: fmchen@m.scnu.edu.cn

26   Kwun Nam Hui, E-mail: bizhui@um.edu.mo

1 **Abstract**

2 Prussian blue analogues (PBAs) have emerged as efficient catalysts for oxygen

3 evolution reaction (OER) due to their porous structure with well-dispersed active sites.

4 However, Co-based PBA (Co-PBA) electrocatalysts are characterized by moderate

5 OER kinetics. In this study, we developed a facile high-yield strategy to fabricate

6 defective Co-PBA (D-Co-PBA) with [Fe(CN)$_6$] vacancies and exposed Co (III) active

7 sites by post-oxidation treatment of the pristine Co-PBA with aqueous H$_2$O$_2$. Rietveld

8 refinement results show that the lattice parameter (a) and unit-cell volume (V) of

9 D-Co-PBA are smaller than those of the pristine Co-PBA, thereby confirming the

10 generation of [Fe(CN)$_6$] vacancies. Density functional theory calculations reveal that

11 the [Fe(CN)$_6$] vacancy can effectively regulate the electronic structure of D-Co-PBA;

12 this condition reduces the reaction barrier of the rate-determining step toward OER. In

13 OER, the D-Co-PBA catalyst achieves a lower overpotential of 400 mV at a current

14 density of 10 mA cm^{-2}, which is superior to that of Ir/C (430 mV) and Co-PBA (450

15 mV). A hybrid sodium-air battery assembled with Pt/C and D-Co-PBA catalysts

16 displays a discharge voltage of 2.75 V, an ultralow charging–discharging gap of 0.15

17 V, and a round-trip efficiency of 94.83% on the 1000th cycle at the current density of

18 0.01 mA cm^{-2}. This study is highly promising for large-scale production of affordable

19 and effective PBA-based materials with desirable OER activity for metal-air batteries

20 and water-alkali electrolyzers, thus helping achieve the goal of sustainability.

21 **Keywords:** Prussian blue analogues, [Fe(CN)$_6$] vacancies, surface electronic

22 configuration, aqueous sodium-air battery

2

1 **Introduction**

2   The rapid development of zero-emission vehicles powered by hydrogen or

3 electricity for net-zero society has stimulated an increasing demand for

4 high-performance energy storage and conversion technologies, such as fuel cells [1,

5 2], water-alkali electrolyzers [3, 4], and metal-air batteries [5-7]. The performances of

6 these technologies highly depend on catalysts' activity toward oxygen evolution

7 reaction (OER). Thus, the exploration of highly efficient and cost-effective catalysts

8 for OER is crucial. In recent years, Prussian blue analogues (PBAs) with a general

9 structure of $A_x M[Fe(CN)_6]_y \cdot mH_2O$ ($0 \leq x \leq 2$, $y <1$) (A: alkaline metal, M: transition

10 metal) have emerged as efficient catalysts for OER due to well-dispersed active sites

11 and charge states [8-12]. In particular, Co-based Prussian blue analogues (Co-PBAs)

12 are robust and stable in a broad pH range due to the stabilization of the

13 hexacyanoferrate group. However, most reported Co-PBAs exhibit unsatisfactory

14 OER activities because of the slow reaction kinetics of multi-electron transfer steps in

15 OER processes, resulting in high overpotential [13, 14]. Therefore, it is imperative to

16 develop a facile approach to improve the OER activities of Co-PBAs.

17   According to the Sabatier principle, the best catalyst should bond atoms or

18 molecules with an intermediate strength; an extremely weak interaction is not

19 conducive to the activation of reactants and extremely strong interaction is not

20 beneficial for the desorption of products. Previous experimental studies have

21 demonstrated that a regulated oxidation state of Co(III) active sites lower the

3

1 adsorption energy of reaction intermediates [15]. Regulating the surface charge

2 properties of catalysts by creating defects is a recognized approach to enrich the

3 catalytic sites with improved activity. Recently, O- and N-enriched PBA materials

4 possessing abundant $[Fe(CN)_6]$ vacancies have been prepared through a plasma

5 treatment approach [9, 16]. These PBA materials with $[Fe(CN)_6]$ vacancies possessed

6 high OER activity due to the exposure of the Co (III) active sites, which decreased the

7 reaction barrier of the rate-determining step toward OER. Studies have shown that

8 Co(III) active sites are favorable for enhanced OER compared to Co(II) owing to its

9 enhanced electrical conductivity and electrons transfer during OER processes [17-19].

10 Unfortunately, the reported plasma approach requires sophisticated equipment and

11 high operation cost, making it less competitive for large-scale productions. As a result,

12 a cost-effective and high-yield approach to prepare efficient PBAs for OER has yet to

13 be developed and remains challenging. Moreover, the interplay between the $[Fe(CN)_6]$

14 vacancy on the charge distribution of Co-PBA and underlying improved OER activity

15 is not sufficiently understood. This knowledge gap has to be addressed to unleash the

16 potential of Co-based PBAs in many industrial energy storage and conversion

17 technologies. This study is the first to report a facile high-yield post-oxidation

18 strategy for creating $[Fe(CN)_6]$ vacancies and simultaneously exposing Co (III) active

19 sites in Co-PBA (D-Co-PBA) by breaking bonds of iron carbon–nitrogen–cobalt units

20 by stirring the synthesized Co-PBA in H_2O_2 solution. Density functional theory (DFT)

21 calculations reveal that the $[Fe(CN)_6]$ vacancy, as confirmed by Rietveld refinement

22 analysis, effectively regulates the electronic structure of D-Co-PBA, thereby reducing

4

the reaction barrier of the rate-determining step toward OER. A hybrid sodium-air

battery (HSAB), which utilizes Pt/C and D-Co-PBA catalysts in the air cathode, was

evaluated for its charge–discharge polarization under various discharge current

densities (0.01–4 mA cm^{-2}), compared with the HSAB using commercial Pt/C and

Ir/C catalysts in the air cathode.

Experimental

Synthesis of Co-PBA. First, 6.0 mmol of Co(NO$_3$)$_2$ • 6H$_2$O and 4.0 mmol of

Na$_4$[Fe(CN)$_6$] was dissolved in 50 mL deionized (DI) water to form solutions A and B,

respectively. Thereafter, solution A was added into solution B to obtain a brown

precipitate, which was then collected by centrifugation, washed, and dried overnight

at 80 °C in a vacuum oven.

Synthesis of D-Co-PBA. The prepared Co-PBA was continuously stirred in 50 ml DI

water under 600 rpm for 0.5 h to obtain a highly dispersed solution. Then, 5 ml of

H$_2$O$_2$ was added to the solution to synthesize D-Co-PBA by the following equation:

$$Fe[(CN)_6]^{4-} + H_2O_2 + H_2O \leftrightarrow HCO_3^- + NH_3 + Fe^{3+}. \tag{1}$$

After another 0.5 h of stirring, the sample was washed thrice with DI water.

Characterizations. Rigaku SmartLab X-ray diffractometer (SmartLab, Rigaku) was

used to obtain powder X-ray powder diffraction (PXRD) patterns. Field emission

scanning electron microscopy (Sigma, Zeiss) was performed to analyze the

morphologies and composition samples. Transmission electron microscopy (TEM)

and selected area electron diffraction (SAED) was performed using a microscope

1   (Talos F200X, FEI). Raman spectra were obtained with a 320 nm laser by using a

2   Horiba LABHRev-UV system. X-ray photoelectron spectroscopic (XPS) studies were

3   performed using a Thermo instrument (Thermo Fisher). Fourier transform infrared

4   spectroscopy (FT-IR) was conducted with on Nicolet 6700 spectrometer (Thermo

5   Scientific). The specific surface area of samples was tested by a nitrogen adsorption–

6   desorption method (Micromeritics 3Flex).

7   **Electrochemical Measurements.** To obtain the homogeneous catalyst inks, 10 mg

8   catalyst was dispersed by ultrasonication for 30 min in 1 ml solution containing 940

9   µL ethanol, 40 µL H_2O, and 20 µL 5% Nafion solution. To obtain the desired working

10 electrode, 20 µL of the prepared inks were dropped onto a glassy carbon (GC)

11 electrode. The electrochemical performance was measured by a CHI 760E

12 electrochemical workstation (Shanghai Chenhua, China) in nitrogen saturated 1 M

13 KOH. Here, the GC electrode with a layer of catalysts, Ag/AgCl (saturated KCl

14 solution), and Pt wires was used as working electrode, reference, and counter

15 electrodes. All the electrochemical performance was recorded at a rotating speed of

16 1600 rpm with a sweep rate of 10 mV s^{-1}. Rotation ring disk electrodes (RRDE) were

17 used to study the mechanism of the OER process in O_2-saturated 1 M KOH solution.

18 To obtain the content of the intermediates (HO^{2-}), the ring potential was fixed at 1.5 V

19 vs. RHE. The Faradaic efficiency (ε) was calculated by obtaining the ring potential at

20 0.4 V (vs. RHE) and disk current at 600 µA in N_2-saturated 1 m KOH solution.

21 $\varepsilon = \frac{I_r}{I_D \times N}$,   (2)

1 where I_r stands for ring current, I_d represents disk current, and N is collection

2 efficiency (0.38).

3 Cyclic voltammetry (CV) curves at different scan rates (10–80 mV s^{-1}) were recorded

4 to reflect the electrochemical surface area (ECSA) of samples by measuring the

5 double layer capacitance as follows:

6 $$C_{dl} = \frac{I_c}{v},$$ (3)

7 where C_{dl} represents double-layer capacitance, I_c is charging current, and v is scan

8 rate.

9 The turnover frequency (TOF) was calculated as follows:

10 $$TOF = \frac{J \times A}{4 \times m \times F},$$ (4)

11 where J is the current density at an overpotential of 450 mV, A is the area of the

12 electrode, m is the number of moles of the active materials deposited onto the

13 electrode, and F is Faraday constant (96485 C mol^{-1}).

14 **Assembly of hybrid sodium-air battery (HSAB):** A liquid anode was prepared

15 based on our previous work.[6] The liquid anode was prepared by dissolving sodium

16 metal in a solution of tetraethylene glycol dimethyl ether. $Na_3Zr_2Si_2PO_{12}$ solid

17 ceramic with ionic conductivity of 8.9×10^{-4} S cm^{-1} at room temperature was utilized

18 as a separator. Oxygen-saturated 0.1 M NaOH solution with O_2 (99.999%) was fed for

19 30 mins as an aqueous electrolyte and sealed in a tube. For the preparation of air

20 electrode, the catalyst, active carbon, and sodium sulfate anhydrous with a weight

1   ratio of 0.1:0.03:0.02 g were milled with polytetrafluoroethylene (60 wt.%, 0.2 mL) to

2   produce a uniform mixture. Ethanol was used as an organic solvent that was added

3   into the mixture to produce a paste. The catalytic layer was pressured to 0.3 mm by

4   the roller press from the paste. The nickel foam was adopted as a current collector,

5   and the catalytic layer was laminated on one side by the rolling method. The HSABs

6   were assembled in a glove box filled with high-purity argon (O_2 and H_2O < 0.1 ppm),

7   which consists of liquid anode | NASICON | catholyte | catalytic cathode. The

8   electrochemical performance of the HSABs was tested at room temperature.

9   **Calculation methods**

10 All calculations of core electrons on the valence electron density were performed

11 using the projector augmented wave (PAW) potential and a plane-wave DFT as

12 implemented in the Vienna *Ab Initio* Simulation Package (VASP 5.4.1) [20, 21]. The

13 bulk and surface properties of PBA were optimized by Perdew–Burke–Ernzerhof

14 functional within the generalized gradient approximation [22, 23]. The 3×3×1

15 Monkhorst–Pack *k*-point sampling was used to optimize the bulk lattice constants, a =

16 10.12, b = 10.12, c = 33.31 and α = β = γ = 90. All elements adopt the

17 pseudo-potential document recommended by the VASP official website. Furthermore,

18 450 eV was set as the cut-off energy for plane-wave basis functions with a 1×10^{-4} eV

19 convergence criterion for the energy [24]. The convergence criterion for the force of

20 atoms in the system was set as 0.03 eV A^{-1}. A vacuum distance of 15 Å was set for

21 PBA (200) to ensure sufficient vacuum to avoid interactions between two periods.

22 Van der Waals interactions in the systems were described based on Grimme's DFT-D3

1   scheme [25, 26]. We also considered spin polarization in all the calculations.

2   **Results and discussion**

3   The Co-PBA was prepared by a co-precipitation method as in previous literature

4   (Fig. 1a) [9, 27]. The XRD pattern indicates that the as-prepared Co-PBA corresponds

5   to $Co_3[Fe(CN)_6]_2$ crystal structure (JCPDS#86-0502) [9, 27]. D-Co-PBA was obtained

6   by performing the post-oxidation treatment with H_2O_2 solution (Fig. 1a). The XRD

7   pattern of the D-Co-PBA remains identical to those of Co-PBA, and slight peaks shift

8   to higher angles were observed. To explain the effect of $[Fe(CN)_6]$ vacancies on the

9   structural properties of Co-PBA, we used FullProf Suite (UT-Battelle) to analyze the

10   Rietveld refinement using the collected room-temperature PXRD patterns of the

11   Co-PBA and D-Co-PBA material data [28]. The refinement results of the Co-PBA and

12   D-Co-PBA materials (Fig. S1) show that the lattice parameter (a) and unit-cell volume

13   (V) of D-Co-PBA are both smaller than that of Co-PBA, which indicates that the

14   decrease in the lattice space is attributed to the generation of the $[Fe(CN)_6]$ vacancies.

15   The lattice parameter values are calculated from the refinements and are found to be a

16   = 10.2436(21) Å and 10.1982(3) Å for Co-PBA and D-Co-PBA, respectively (Table

17   S1). The surface morphology of Co-PBA and D-Co-PBA were examined with

18   FESEM. The results show uniform nanoparticles with the size of 50 nm and smooth

19   surface (Fig. 1c and S2), indicating that the post-oxidation treatment did not change

20   the structure and surface property of Co-PBA. TEM images of the as-prepared

21   D-Co-PBA (Fig. 2a) also show a highly uniform spherical morphology with an

22   average size of 50 nm. HRTEM images in Fig. 2b show a set of lattice fringes with

1   interplane distances of 0.252 nm corresponding to the (200) planes of orthorhombic

2   Co-PBA [9]. The inserted HRTEM images of D-Co-PBA display crystalline domains

3   with the discontinuous atomic arrangement (zones 1 and 2), as further demonstrated

4   by the peak valleys of the atomic intensity profile, suggesting the presence of

5    $[Fe(CN)_6]$ vacancies (insets of Fig. 2b and S3). The crystallinity of D-Co-PBA was

6   also investigated by the SAED pattern, and three circles indexed to the (200), (220),

7   and (400) planes were observed [9] (Fig. 2c). High-angle annular dark-field scanning

8   TEM (HAADF-STEM) indicates that D-Co-PBA also has a nanoparticle structure, as

9   shown in Fig. 2d. Energy-dispersive X-ray spectroscopy in Figs. 2e–h suggest that Co,

10   Fe, C, and N elements were homogeneously distributed in all of the materials.

11   Electron paramagnetic resonance (EPR) spectrometry was performed to verify the

12   defect and presence of $[Fe(CN)_6]$ vacancies in the lattice. As shown in Fig. S4, the

13   samples show a symmetrical signal at the magnetic field corresponding to $g = 2.00$,

14   indicating the presence of $[Fe(CN)_6]$ vacancies in the lattice. We can observe that the

15   EPR intensity of D-Co-PBA is much larger than that of Co-PBA, suggesting that

16   additional $[Fe(CN)_6]$ vacancies are created in D-Co-PBA.

17   The surface property and chemical states of Co-PBA and D-Co-PBA were further

18   examined by XPS. XPS survey spectra identify the presence of Co, Fe, C, and N for

19   Co-PBA and D-Co-PBA (Fig. S5 and Table S2), suggesting no significant change in

20   the composition of materials. Specifically, the Co $2p^{3/2}$ core level region of Co-PBA

21   shows two peaks at 781.5 eV and 782.6 eV (Fig. 3a), which corresponds to the Co^{3+}

22   and Co^{2+} states [9, 29], respectively. A positive shift to high binding energy is

1   observed from the fitted Co^{3+} and Co^{2+} peaks in D-Co-PBA after post-oxidation. This

2   condition is mainly attributed to the combination of exposed Co and H_2O molecules.

3   The oxidative property of $[Co(CN)_6]^{3-}$ was less than that of $[Co(H_2O)_6]^{3+}$, which

4   enables the negatively charged CN^- group to effectively stabilize Co^{3+} [8]. Therefore,

5   the electron-withdrawing oxo group makes the Co site more oxidative and favorable

6   for OER, as demonstrated in molecular complexes. The oxidation states of Co are

7   quantitatively corroborated by the fitted ratio of Co^{3+} and Co^{2+} in Co-PBA and

8   D-Co-PBA (Table S2), indicating that more Co^{3+} exposed to the surface and the

9   chemical environment of Co ion was modified. The Fe 2p spectra (Fig. 3b) show two

10   main peaks at 709.9 eV and 708.3 eV in Fe $2p^{3/2}$ spectrum, which correspond to the

11   Fe^{3+} and Fe^{2+} species [9, 30], respectively. Similar to the Co 2p spectra, the binding

12   energies of Fe peak also shift to higher energy, suggesting more oxidized Fe atoms in

13   D-Co-PBA materials. This condition may be attributed to the introduction of $[Fe(CN)_6]$

14   vacancies and partial oxidation of Fe^{2+} caused by H_2O_2. According to the XPS results,

15   the specific formula of Co-PBA and D-Co-PBA is estimated at $Co_3[Fe_{1.1}(C_{0.22}N_{0.1})_6]_2$

16   and $Co_3[Fe_{0.99}(C_{0.2}N_{0.08})_6]_2$, respectively, and the content of $[Fe(CN)_6]$ decreased from

17   96.09% to 87.04%, indicating generation of $[Fe(CN)_6]$ vacancies. Fourier transform

18   infrared spectroscopy (FTIR) was performed to confirm the oxidation states and spin

19   state of metal active sites [29, 31-34]. As shown in Fig. 3c, both Co-PBA and

20   D-Co-PBA display a narrow and intense band centered at 2106 cm^{-1}, which is

21   attributed to Co(III)-CN [35]. Notably, the Co-CN peak of D-Co-PBA is increased

22   compared with Co-PBA, indicating higher oxidation of Co atoms in D-Co-PBA [9,

1 35]. Compared with Co-PBA, the position of the Co-CN peak of D-Co-PBA shifts to

2 a higher wavenumber, indicating the electron transfer from the metal center to the

3 antibonding π^* orbital of the cyanide group [9]. Thus, the results signify a higher

4 oxidation state of the Co metal (Co III) during the formation of D-Co-PBA. The work

5 function of D-Co-PBA and Co-PBA was measured by ultraviolet photoelectron

6 spectroscopy (UPS). Fig. 3d shows that D-Co-PBA possesses a lower work function

7 of 4.62 eV compared with that of Co-PBA (4.68 eV), indicating improved electronic

8 conductivity for electron transfer to and from the active sites and therefore superior

9 catalytic capability [36-38].

10 The electrocatalytic OER activities of the D-Co-PBA and Co-PBA toward OER

11 were evaluated in 1 M KOH solution. Linear sweep voltammetry (LSV) polarization

12 curves were first performed on glass carbon (GC) electrodes with different samples,

13 as shown in Fig. 4. Notably, a smaller onset potential of 1.57 V was observed for

14 D-Co-PBA compared with those of Co-PBA (1.65 V) and Ir/C (1.62 V), indicating

15 best OER performance of D-Co-PBA (Fig. 4a and Table S3). Besides, Co-PBA

16 required an overpotential of 450 mV to reach the current density of 10 mA cm^{-2},

17 whereas this value decreased to 400 mV for D-Co-PBA and was even superior to Ir/C

18 (430 mV) (Fig. 4b). The enhanced OER performance of D-Co-PBA was attributed to

19 the destructive impact of the post-oxidation treatment, which promoted the breakage

20 of the Co=N coordination bond, and the abundant Co (III) species were exposed on

21 the surface. Furthermore, the specific activity (by BET normalization) of D-Co-PBA

22 was higher than that of Co-PBA, indicating the positive effect of $[Fe(CN)_6]$ vacancies
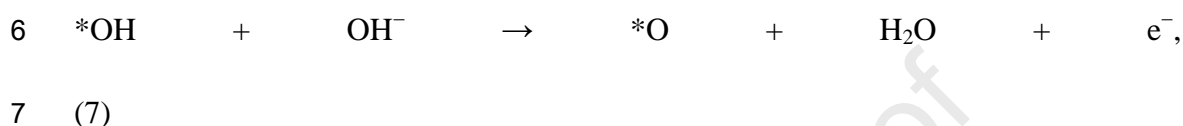
1   (Figs. 4c and S6). 10 mM potassium thiocyanate (KSCN) in 1 M KOH was used to

2   confirm the acceptable Co active sites instead of C and N atoms by complexing with

3   the Co atoms. A negligible OER current density was observed from the LSV

4   polarization curve in Fig. S7, suggesting that Co acted as the real electrocatalytic

5   active sites for OER instead of C and N atoms. A steady-state Tafel plot is depicted in

6   Fig. 4d to evaluate the kinetics of catalysts. A much smaller Tafel slope of 70.3 mV

7   dec^{-1} was observed for D-Co-PBA compared with the original Co-PBA (108.8 mV

8   dec^{-1}), indicating high OER kinetics for D-Co-PBA. To further study the electrode

9   reaction kinetics, electrochemical impedance spectroscopy (EIS) was conducted on

10   the materials. Nyquist plots reveal a dramatically decreased R_{ct} value (3.1 Ω) for

11   D-Co-PBA compared with Co-PBA (3.8 Ω) (Fig. 3e), which suggests a rapid charge

12   transfer in the D-Co-PBA electrode. This result can also be demonstrated by Bode

13   plots in Fig. S8, which shows the smallest resistance in the tested frequency range for

14   D-Co-PBA compared with Co-PBA. Double-layer capacitances (C_{dl}) were also

15   calculated to reflect the electrochemical active surface area (ECSA) of D-Co-PBA and

16   Co-PBA (Fig. S9). The results indicated that D-Co-PBA possessed a larger C_{dl} of

17   177.2 mF cm^{-2} than that of Co-PBA (83.9 mF cm^{-2}), revealing that D-Co-PBA

18   possessed a higher density of catalytic active sites (Fig. 4f). The increased ECSA was

19   attributed to the introduction of $[Fe(CN)_6]$ vacancies, which improved the ion

20   exchange between the electrolyte and catalytically active sites. The TOF of

21   D-Co-PBA was determined to be 0.041 s^{-1} at an overpotential of 450 mV, which was

22   larger than the TOF of Co-PBA (0.015 s^{-1}), indicating a greater number of exposed

13

1   active sites due to the generation of [Fe(CN)$_6$] vacancies. To investigate the stability

2   of D-Co-PBA under continuous operation, we recorded chronoamperometric curves,

3   which show that D-Co-PBA affords a much larger current retention (72%, 10000 s)

4   than that of the benchmark Ir/C (45%, 10000 s), signaling the outstanding durability

5   of D-Co-PBA for OER electrocatalysis (Fig. S10).

6   To understand the electron transfer theory of OER, we performed RRDE with a

7   ring potential of 1.5 V (vs. RHE) under the OER condition (1600 rmp). Fig. 4g shows

8   that a small ring current of 8–10 µA was observed for D-Co-PBA compared with its

9   disk current, which suggests the possible formation of H$_2$O$_2$ during OER. In addition,

10   the observed ring current drops rapidly when the disk potential reaches as high as 1.5

11   V, indicating that few peroxide products were generated even at a high potential range

12   [39]. Furthermore, no significant current was detected at the Pt ring (Fig. 4h), thereby

13   verifying a favorable four-electron pathway due to negligible peroxide oxidation. To

14   demonstrate that the significantly increased current results from water oxidation

15   instead of peroxide oxidation, we also calculated the Faradaic efficiency (ε). As

16   shown in Fig. 4i, the ring current was observed to be 200 µA when the disk current

17   was applied at 600 µA, resulting in high Faradaic efficiency of 92%.

18   Inspired by the remarkable OER performance of the synthesized catalysts, we

19   further investigated the electronic configurations and related [Fe(CN)$_6$] vacancy

20   through DFT calculations. The (200) surface corresponding to the edge of the

21   Co-PBA structure is considered for the DFT calculation (Fig. 5a). To simulate the

22   oxygen vacancy, a [Fe(CN)$_6$] group was removed from the sublayer of (200), and then

14

1   the exposed Co site became the active site for OER. The structures of Co-PBA with

2   and without [Fe(CN)$_6$] vacancy are presented in Fig. S11. The calculated Gibbs free

3   energy of elementary coordinate steps and an overpotential for OER in alkaline media
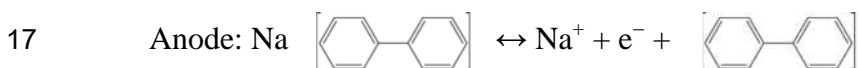
4   are based on the following 4e⁻ mechanism [40, 41]:

5   $* + OH^- (aq) \rightarrow *OH + e^-$,   (6)

6   $*OH \quad + \quad OH^- \quad \rightarrow \quad *O \quad + \quad H_2O \quad + \quad e^-$,

7   (7)

8   $*O + OH^- \rightarrow *OOH + e^-$,   (8)

9   $*OOH + OH^- \rightarrow O_2 + H_2O + e^- + *$.   (9)

10 The free energy pathways of the OER process are also calculated by simulating the

11 adsorption energies of intermediates, as depicted in Fig. 5a–c. Intermediate *OH, *O,

12 and *OOH are attached to the Co active site with a single bond through oxygen (Figs.

13 5a and S12). Figure 5b–c shows the OER Gibbs free energy ($\varDelta G$) diagram for the

14 (200) surface of Co-PBA and D-Co-PBA with correlative intermediates at different

15 reaction steps. The OER rate-determining step was found to be the formation of

16 *OOH from the *O for the Co-PBA and the formation of *OH for the D-Co-PBA. To

17 verify the active sites responsible for the enhanced OER kinetics, we selected Fe

18 atoms in the (200) crystal plane of the D-Co-PBA as active sites for DFT calculations.

19 The results revealed that the overpotential (0.49 V) in the Fe atoms (Fig. S13) is

20 higher than that in the Co sites (0.43 V) of D-Co-PBA (Fig. 5c), suggesting that Co

21 atoms have more favorable kinetics toward OER compared with Fe atoms. By

22 comparing the free energy plots in Figs. 5b–c, we found that the Co active sites on the

15

1 (200) surface of the D-Co-PBA showed a lower Gibbs free energy (1.66 eV vs.

2 overpotential of 0.43 V) of the rate-determining step than that of Fe (1.75 eV vs.

3 overpotential of 0.52 V) and Co (2.33 eV vs. overpotential of 1.01 V) active sites on

4 the surface Co-PBA (Fig. S14), thereby confirming that Co active sites are favorable

5 OER kinetics in D-Co-PBA.

6 We studied the electronic structure of Co-PBA and D-Co-PBA to further

7 understand the effect of $[Fe(CN)_6]$ vacancy on OER performance. The density of state

8 (DOS) functions of Co-PBA and D-Co-PBA were calculated, as shown in Fig. 5d. For

9 the Co-PBA materials, the surface Co atoms without $[Fe(CN)_6]$ vacancies indicated

10 that the major spin-down components become conductive as evidenced by the DOS

11 found around the Fermi energy level, which verifies that the Co-PBA without

12 $[Fe(CN)_6]$ vacancies already have a half-metal-like conductivity [42]. However, the

13 formation of $[Fe(CN)_6]$ vacancies in D-Co-PBA further increases the spin-up DOS

14 near the Fermi level compared with that of Co-PBA and results in a decrease of the

15 spin-down DOS. The asymmetry of the DOS in the valence band leads to the

16 generation of magnetic moments, which suggest that $[Fe(CN)_6]$ vacancies lead to the

17 formation of the metallic performance of the D-Co-PBA, thereby benefiting their

18 charge transfer capability during electrochemical reactions [42]. These calculations

19 agree well with the EIS measurements (Fig. 4e) in which a much lower charge

20 transfer resistance of the D-Co-PBA than that of the Co-PBA implies more favorable

21 charge transport kinetics. The *p*-band centers of Co-PBA and D-Co-PBA are also

22 calculated for the OER catalytic activity. The calculated *p*-band centers of the cyano

1   group in D-Co-PBA (–0.21 eV) shift away from the Fermi level compared with those

2   of Co-PBA (–0.18 eV), suggesting higher OER catalytic activity [43-47]. This

3   enhanced OER activity is due to the $[Fe(CN)_6]$ vacancies on the surface; these

4   vacancies promote Co 3d $e_g\uparrow$ near the top of the valance band and the electron

5   transfer to the p-band of the cyano group, thereby enhancing OER performance (Fig.

6   5d) [43]. The electron density contour maps of Co were also studied to investigate the

7   electronic structure of the Co-PBA before and after generating the $[Fe(CN)_6]$

8   vacancies, as shown in Fig. 5e. The electronic density of Co decreased after the

9   introduction of $[Fe(CN)_6]$ vacancies demonstrating a higher valence state, which

10   agreed with our XPS results.

11   To show the electrocatalytic performance for an actual application, we fabricated

12   an HSAB with the air electrode consisting of D-Co-PBA (acting as OER) and Pt/C

13   (acting as ORR) electrocatalysts (Fig. 6a) [48-50]. The battery reaction during the

14   charge and discharge process is as follows: sodium ion transfer to the catholyte and

15   back for discharge and charge, respectively, which is distinguished from the

16   traditional HSAB with sodium metal [51].

17   Anode: Na $\left[\bigcirc\!\!-\!\!\bigcirc\right]$ $\leftrightarrow$ Na$^+$ + e$^-$ + $\left[\bigcirc\!\!-\!\!\bigcirc\right]$

18   Cathode: $4OH^- \leftrightarrow 2H_2O + O_2 + 4e^-$

19   Fig. 6b shows the charge–discharge profiles of the HSABs with different

20   catalysts, and ΔV is the voltage gap of the battery. At the current density of 0.01 mA

21   cm^{-2}, the HSAB utilizing D-Co-PBA and Pt/C as the air electrode exhibited a higher

22   discharge voltage of 2.75 V and charge voltage of 2.90 V, resulting in an improved

1   performance with a lower ΔV of 0.15 V compared with that of the reference electrode

2   containing Pt/C+Ir/C (0.23 V). Correspondingly, the 1st cycle round-trip efficiency

3   (charge-to-discharge voltage ratio) of the HSAB using D-Co-PBA and Pt/C reached

4   94.83% compared with Pt/C+Ir/C (93.2%). Polarization curves of the HSAB using

5   D-Co-PBA and Pt/C also indicate a relatively lower overpotential gap, suggesting

6   superior catalytic activity than that using Pt/C+Ir/C (Fig. 6c). To demonstrate the

7   feasibility of the D-Co-PBA catalyst in the full-cell configuration, we operated the

8   battery under continuous 20 min per charge–discharge at 0.01 mA cm^{-2} curves up to

9   1000 cycles, as shown in Fig. 6d. Minimal decay in terminal discharge voltage was

10   detected during the 1000 cycles,   indicating excellent reversibility of the battery.

11   Notably, a slight voltage increase from 2.78 V to 2.81 V (0.03 V) was observed during

12   the first 100 cycles (Fig. 6e) because of the decreased interface resistance between

13   NASICON and liquid anode, between NASICON and NaOH electrolyte, and between

14   NaOH electrolyte and air electrode during the operation. However, no obvious change

15   in voltage was obtained during the long-term charge–discharge process of the

16   batteries. Overall, the HSAB shows a slight decrease in discharge voltage (by 0.13%)

17   during the 1000 cycles (Fig. 6e), suggesting an acceptable cyclability in practical

18   application. The performance of HSAB was compared with those of other reported

19   batteries (Table S4).

20   **Conclusions**

21   We demonstrated a facile large-scale approach to synthesize the D-Co-PBA

1   catalyst with rich [Fe(CN)$_6$] vacancies and exposed Co (III) sites through a

2   post-oxidation treatment of the pristine Co-PBA with aqueous H$_2$O$_2$. Rietveld

3   refinement analysis confirms the generation of [Fe(CN)$_6$] vacancies in the D-Co-PBA

4   catalyst. DFT calculations reveal that the electronic structure of Co-PBA can be tuned

5   by [Fe(CN)$_6$] vacancy, decreasing the energy barrier toward OER, and thereby

6   improving OER kinetics. An HSAB, which utilized Pt/C (for ORR) and D-Co-PBA

7   (for OER) catalysts in the air cathode, exhibited better performance with a lower

8   charging–discharging gap (0.15 V) at the current density of 0.01 mA cm^{-2} compared

9   with that of the same device containing commercial Pt/C and Ir/C catalysts (0.23 V).

10   This study proposed a new synthesis strategy for producing PBA catalysts with high

11   OER activity for a wide range of valuable applications in energy storage and

12   conversion.

13   **Conflicts of interest**

14   There are no conflicts to declare.

Reference

[1] W. Yang, X. Wang, R. Rossi, B.E. Logan, Low-cost Fe–N–C catalyst derived from Fe (III)-chitosan hydrogel to enhance power production in microbial fuel cells, Chem Eng J, 380 (2020) 122522.

[2] S. Xin, J. Shen, G. Liu, Q. Chen, Z. Xiao, G. Zhang, Y. Xin, Electricity generation and microbial community of single-chamber microbial fuel cells in response to Cu2O nanoparticles/reduced graphene oxide as cathode catalyst, Chem Eng J, 380 (2020) 122446.

[3] P.W. Menezes, A. Indra, I. Zaharieva, C. Walter, S. Loos, S. Hoffmann, R. Schlögl, H. Dau, M. Driess, Helical cobalt borophosphates to master durable overall water-splitting, Energy & Environmental Science, 12 (2019) 988.

[4] J. Shan, T. Ling, K. Davey, Y. Zheng, S.-Z. Qiao, Transition-Metal-Doped RuIr Bifunctional Nanocrystals for Overall Water Splitting in Acidic Environments, Advanced Materials, 31 (2019) 1900510.

[5] Y. Wu, X. Qiu, F. Liang, Q. Zhang, A. Koo, Y. Dai, Y. Lei, X. Sun, A

metal-organic framework-derived bifunctional catalyst for hybrid sodium-air batteries, Applied Catalysis B: Environmental, 241 (2019) 407.

[6] F. Liang, X. Qiu, Q. Zhang, Y. Kang, A. Koo, K. Hayashi, K. Chen, D. Xue, K.N. Hui, H. Yadegari, X. Sun, A liquid anode for rechargeable sodium-air batteries with low voltage gap and high safety, Nano Energy, 49 (2018) 574.

[7] J. Zhu, T. Qu, F. Su, Y. Wu, Y. Kang, K. Chen, Y. Yao, W. Ma, B. Yang, Y. Dai, F. Liang, D. Xue, Highly dispersed Co nanoparticles decorated on a N-doped defective carbon nano-framework for a hybrid Na–air battery, Dalton T, 49 (2020) 1811.

[8] Y. Wang, J. Ma, J. Wang, S. Chen, H. Wang, J. Zhang, Interfacial Scaffolding Preparation of Hierarchical PBA-Based Derivative Electrocatalysts for Efficient Water Splitting, Advanced Energy Materials, 9 (2019) 1802939.

[9] Y. Guo, T. Wang, J. Chen, J. Zheng, X. Li, K. Ostrikov, Air Plasma Activation of Catalytic Sites in a Metal-Cyanide Framework for Efficient Oxygen Evolution Reaction, Advanced Energy Materials, 8 (2018) 1800085.

[10] S. Pintado, S. Goberna-Ferrón, E.C. Escudero-Adán, J.R. Galán-Mascarós, Fast and Persistent Electrocatalytic Water Oxidation by Co–Fe Prussian Blue Coordination Polymers, Journal of the American Chemical Society, 135 (2013) 13270.

[11] L. Han, P. Tang, Á. Reyes-Carmona, B. Rodríguez-García, M. Torréns, J.R. Morante, J. Arbiol, J.R. Galan-Mascaros, Enhanced Activity and Acid pH Stability of Prussian Blue-type Oxygen Evolution Electrocatalysts Processed by Chemical Etching, Journal of the American Chemical Society, 138 (2016) 16037.

[12] X. Su, Y. Wang, J. Zhou, S. Gu, J. Li, S. Zhang, Operando Spectroscopic

Identification of Active Sites in NiFe Prussian Blue Analogues as Electrocatalysts: Activation of Oxygen Atoms for Oxygen Evolution Reaction, Journal of the American Chemical Society, 140 (2018) 11286.

[13] Y. Wang, Y. Wang, L. Zhang, C.-S. Liu, H. Pang, PBA@POM Hybrids as Efficient Electrocatalysts for the Oxygen Evolution Reaction, Chemistry – An Asian Journal, 14 (2019) 2790.

[14] Z. Chen, B. Fei, M. Hou, X. Yan, M. Chen, H. Qing, R. Wu, Ultrathin Prussian blue analogue nanosheet arrays with open bimetal centers for efficient overall water splitting, Nano Energy, 68 (2020) 104371.

[15] J. Wang, W. Liu, G. Luo, Z. Li, C. Zhao, H. Zhang, M. Zhu, Q. Xu, X. Wang, C. Zhao, Y. Qu, Z. Yang, T. Yao, Y. Li, Y. Lin, Y. Wu, Y. Li, Synergistic effect of well-defined dual sites boosting the oxygen reduction reaction, Energy & Environmental Science, 11 (2018) 3375.

[16] Z.-Y. Yu, Y. Duan, J.-D. Liu, Y. Chen, X.-K. Liu, W. Liu, T. Ma, Y. Li, X.-S. Zheng, T. Yao, M.-R. Gao, J.-F. Zhu, B.-J. Ye, S.-H. Yu, Unconventional CN vacancies suppress iron-leaching in Prussian blue analogue pre-catalyst for boosted oxygen evolution catalysis, Nature Communications, 10 (2019) 2799.

[17] M. Bajdich, M. García-Mota, A. Vojvodic, J.K. Nørskov, A.T. Bell, Theoretical Investigation of the Activity of Cobalt Oxides for the Electrochemical Oxidation of Water, Journal of the American Chemical Society, 135 (2013) 13521.

[18] A. Bergmann, E. Martinez-Moreno, D. Teschner, P. Chernev, M. Gliech, J.F. de Araújo, T. Reier, H. Dau, P. Strasser, Reversible amorphization and the catalytically

active state of crystalline Co3O4 during oxygen evolution, Nature Communications, 6 (2015) 8625.

[19] G. Mattioli, P. Giannozzi, A. Amore Bonapasta, L. Guidoni, Reaction Pathways for Oxygen Evolution Promoted by Cobalt Catalyst, Journal of the American Chemical Society, 135 (2013) 15353.

[20] P.E. Blöchl, Projector augmented-wave method, Phys Rev B, 50 (1994) 17953.

[21] G. Kresse, J. Furthmüller, Efficient iterative schemes for ab initio total-energy calculations using a plane-wave basis set, Phys Rev B, 54 (1996) 11169.

[22] J.P. Perdew, K. Burke, M. Ernzerhof, Generalized Gradient Approximation Made Simple, Physical Review Letters, 77 (1996) 3865.

[23] J.P. Perdew, Y. Wang, Pair-distribution function and its coupling-constant average for the spin-polarized electron gas, Phys Rev B, 46 (1992) 12947.

[24] H.J. Monkhorst, J.D. Pack, Special points for Brillouin-zone integrations, Phys Rev B, 13 (1976) 5188.

[25] S. Grimme, J. Antony, S. Ehrlich, H. Krieg, A consistent and accurate ab initio parametrization of density functional dispersion correction (DFT-D) for the 94 elements H-Pu, The Journal of Chemical Physics, 132 (2010) 154104.

[26] S. Grimme, S. Ehrlich, L. Goerigk, Effect of the damping function in dispersion corrected density functional theory, Journal of Computational Chemistry, 32 (2011) 1456.

[27] N. Moazezi, M.A. Moosavian, Removal of rubidium ions by polyaniline nanocomposites modified with cobalt-Prussian blue analogues, Journal of

Environmental Chemical Engineering, 4 (2016) 2440.

[28] J. Rodríguez-Carvajal, Recent advances in magnetic structure determination by neutron powder diffraction, Physica B: Condensed Matter, 192 (1993) 55.

[29] R.O. Lezna, R. Romagnoli, N.R. de Tacconi, K. Rajeshwar, Cobalt Hexacyanoferrate: Compound Stoichiometry, Infrared Spectroelectrochemistry, and Photoinduced Electron Transfer, The Journal of Physical Chemistry B, 106 (2002) 3612.

[30] M.J. Piernas-Muñoz, E. Castillo-Martínez, O. Bondarchuk, M. Armand, T. Rojo, Higher voltage plateau cubic Prussian White for Na-ion batteries, Journal of Power Sources, 324 (2016) 766.

[31] M. Berrettoni, M. Giorgetti, S. Zamponi, P. Conti, D. Ranganathan, A. Zanotto, M.L. Saladino, E. Caponetti, Synthesis and Characterization of Nanostructured Cobalt Hexacyanoferrate, The Journal of Physical Chemistry C, 114 (2010) 6401.

[32] S. Goberna-Ferrón, W.Y. Hernández, B. Rodríguez-García, J.R. Galán-Mascarós, Light-Driven Water Oxidation with Metal Hexacyanometallate Heterogeneous Catalysts, ACS Catalysis, 4 (2014) 1637.

[33] N.R. de Tacconi, K. Rajeshwar, R.O. Lezna, Metal Hexacyanoferrates: Electrosynthesis, in Situ Characterization, and Applications, Chem Mater, 15 (2003) 3046.

[34] W. Jin, A. Toutianoush, M. Pyrasch, J. Schnepf, H. Gottschalk, W. Rammensee, B. Tieke, Self-Assembled Films of Prussian Blue and Analogues: Structure and Morphology, Elemental Composition, Film Growth, and Nanosieving of Ions, The

1   Journal of Physical Chemistry B, 107 (2003) 12062.

2   [35] J. Song, C. Zhu, B.Z. Xu, S. Fu, M.H. Engelhard, R. Ye, D. Du, S.P. Beckman, Y.

3   Lin, Bimetallic Cobalt-Based Phosphide Zeolitic Imidazolate Framework: CoPx

4   Phase-Dependent Electrical Conductivity and Hydrogen Atom Adsorption Energy for

5   Efficient Overall Water Splitting, Advanced Energy Materials, 7 (2017) 1601555.

6   [36] X. Zhao, F. Li, R. Wang, J.-M. Seo, H.-J. Choi, S.-M. Jung, J. Mahmood, I.-Y.

7   Jeon, J.-B. Baek, Controlled Fabrication of Hierarchically Structured Nitrogen-Doped

8   Carbon Nanotubes as a Highly Active Bifunctional Oxygen Electrocatalyst, Advanced

9   Functional Materials, 27 (2017) 1605717.

10   [37] R. Almeida, A. Banerjee, S. Chakraborty, J. Almeida, R. Ahuja, Theoretical

11   Evidence behind Bifunctional Catalytic Activity in Pristine and Functionalized Al2C

12   Monolayers, Chemphyschem, 19 (2018) 148.

13   [38] X. Yuan, Z. Zhang, Z. Liu, X. Wang, C. Dong, M.S. Riaz, F. Huang, Efficient

14   Co@CoPx core–shell nanochains catalyst for the oxygen evolution reaction, Inorg

15   Chem Front, 5 (2018) 1844.

16   [39] P. Chen, T. Zhou, L. Xing, K. Xu, Y. Tong, H. Xie, L. Zhang, W. Yan, W. Chu, C.

17   Wu, Y. Xie, Atomically Dispersed Iron–Nitrogen Species as Electrocatalysts for

18   Bifunctional Oxygen Evolution and Reduction Reactions, Angewandte Chemie

19   International Edition, 56 (2017) 610.

20   [40] H. Dau, C. Limberg, T. Reier, M. Risch, S. Roggan, P. Strasser, The Mechanism

21   of Water Oxidation: From Electrolysis via Homogeneous to Biological Catalysis,

22   Chemcatchem, 2 (2010) 724.

[41] L.C. Seitz, T.J.P. Hersbach, D. Nordlund, T.F. Jaramillo, Enhancement Effect of Noble Metals on Manganese Oxide for the Oxygen Evolution Reaction, The Journal of Physical Chemistry Letters, 6 (2015) 4178.

[42] B. Liu, Y. Wang, H.-Q. Peng, R. Yang, Z. Jiang, X. Zhou, C.-S. Lee, H. Zhao, W. Zhang, Iron Vacancies Induced Bifunctionality in Ultrathin Feroxyhyte Nanosheets for Overall Water Splitting, Advanced Materials, 30 (2018) 1803144.

[43] A. Grimaud, K.J. May, C.E. Carlton, Y.-L. Lee, M. Risch, W.T. Hong, J. Zhou, Y. Shao-Horn, Double perovskites as a family of highly active catalysts for oxygen evolution in alkaline solution, Nature Communications, 4 (2013) 2439.

[44] Y. Tian, S. Wang, E. Velasco, Y. Yang, L. Cao, L. Zhang, X. Li, Y. Lin, Q. Zhang, L. Chen, A Co-Doped Nanorod-like RuO2 Electrocatalyst with Abundant Oxygen Vacancies for Acidic Water Oxidation, iScience, 23 (2020) 100756.

[45] F. Ando, T. Tanabe, T. Gunji, S. Kaneko, T. Takeda, T. Ohsaka, F. Matsumoto, Effect of the d-Band Center on the Oxygen Reduction Reaction Activity of Electrochemically Dealloyed Ordered Intermetallic Platinum–Lead (PtPb) Nanoparticles Supported on TiO2-Deposited Cup-Stacked Carbon Nanotubes, Acs Appl Nano Mater, 1 (2018) 2844.

[46] F.H.B. Lima, J. Zhang, M.H. Shao, K. Sasaki, M.B. Vukmirovic, E.A. Ticianelli, R.R. Adzic, Catalytic Activity–d-Band Center Correlation for the O2 Reduction Reaction on Platinum in Alkaline Solutions, The Journal of Physical Chemistry C, 111 (2007) 404.

[47] X. Tian, X. Zhao, Y.-Q. Su, L. Wang, H. Wang, D. Dang, B. Chi, H. Liu, E.J.M.

26

Hensen, X.W. Lou, B.Y. Xia, Engineering bunched Pt-Ni alloy nanocages for efficient oxygen reduction in practical fuel cells, Science, 366 (2019) 850.

[48] C. Xu, K. Zhang, D. Zhang, S. Chang, F. Liang, P. Yan, Y. Yao, T. Qu, J. Zhan, W. Ma, B. Yang, Y. Dai, X. Sun, Reversible hybrid sodium-CO2 batteries with low charging voltage and long-life, Nano Energy, 68 (2020) 104318.

[49] M. Hou, F. Liang, K. Chen, Y. Dai, D. Xue, Challenges and perspectives of NASICON-type solid electrolytes for all-solid-state lithium batteries, Nanotechnology, 31 (2020) 132003.

[50] Y. Kang, S. Wang, Y. Liu, K.S. Hui, H. Li, K.W. Ng, F. Liang, J. Geng, X. Hong, W. Zhou, K.N. Hui, Unveiling the Origin of Catalytic Sites of Pt Nanoparticles Decorated on Oxygen-Deficient Vanadium-Doped Cobalt Hydroxide Nanosheet for Hybrid Sodium–Air Batteries, ACS Applied Energy Materials, 3 (2020) 7464.

[51] Y. Kang, F. Liang, K. Hayashi, Hybrid Sodium–Air Cell with Na[FSA–C2C1im][FSA] Ionic Liquid Electrolyte, Electrochimica Acta, 218 (2016) 119.
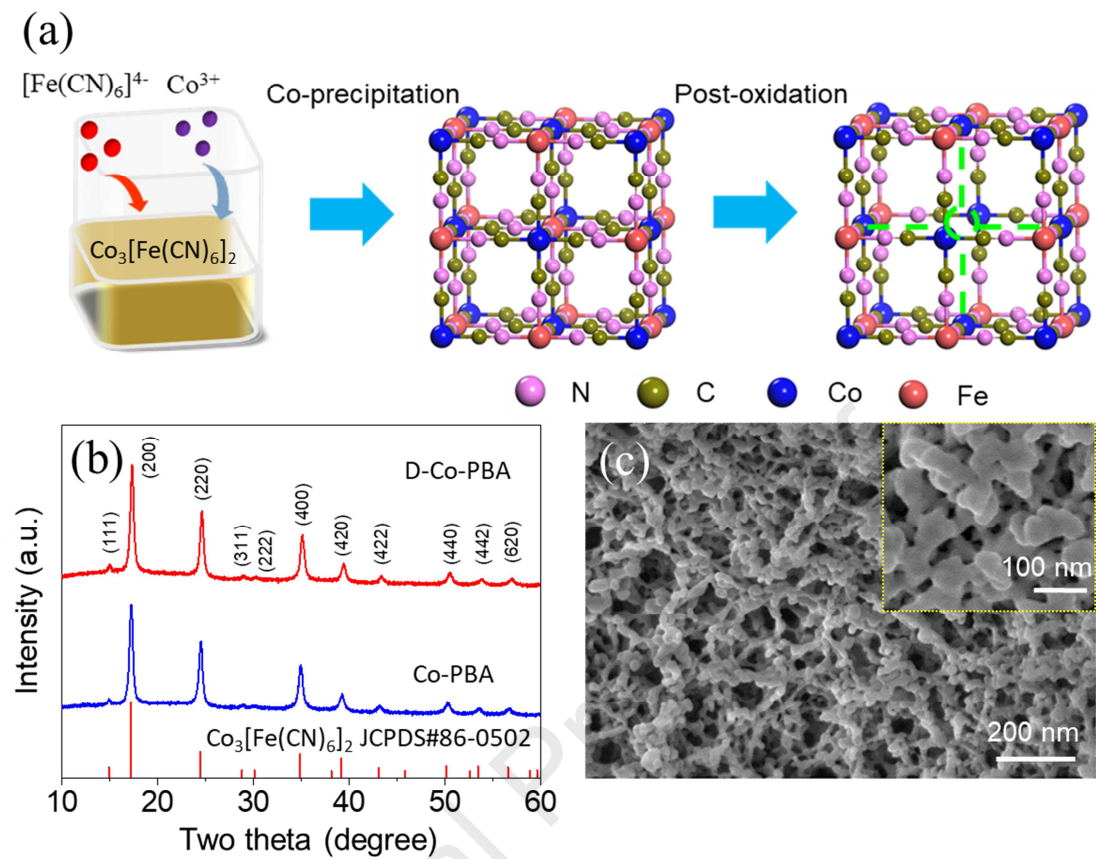
Fig. 1 (a) Schematic of fabrication route of Co-PBA and D-Co-PBA. (b) XRD patterns of Co-PBA and D-Co-PBA. (c) SEM image of D-Co-PBA (inset shows enlarged SEM image).
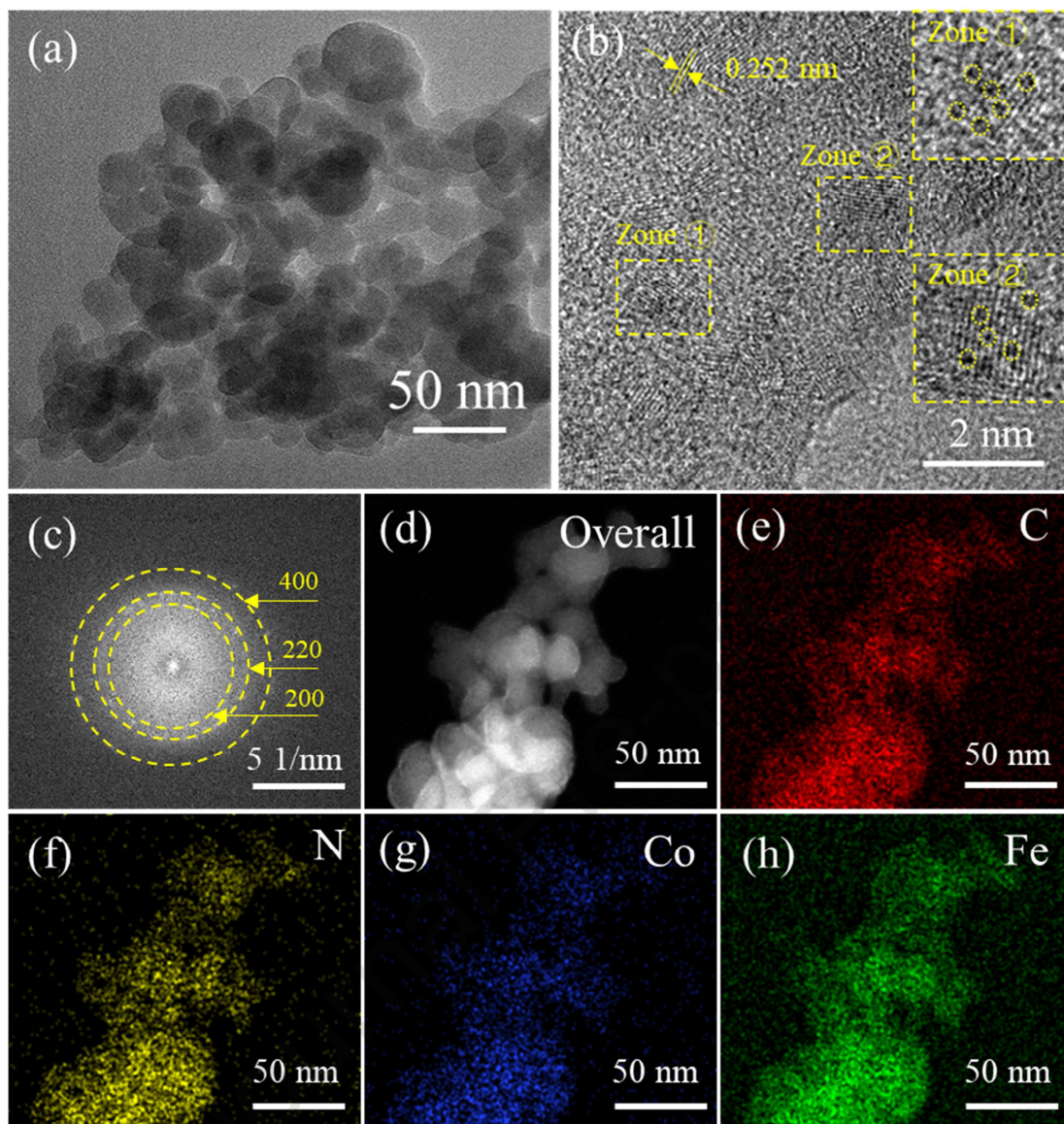
1

Fig. 2 (a) TEM image of D-Co-PBA. (b) HRTEM image of D-Co-PBA (inset shows enlarged HRTEM images). (c) SAED image of D-Co-PBA. (d) HADDF image of D-Co-PBA. (e–f) EDX mapping of D-Co-PBA.
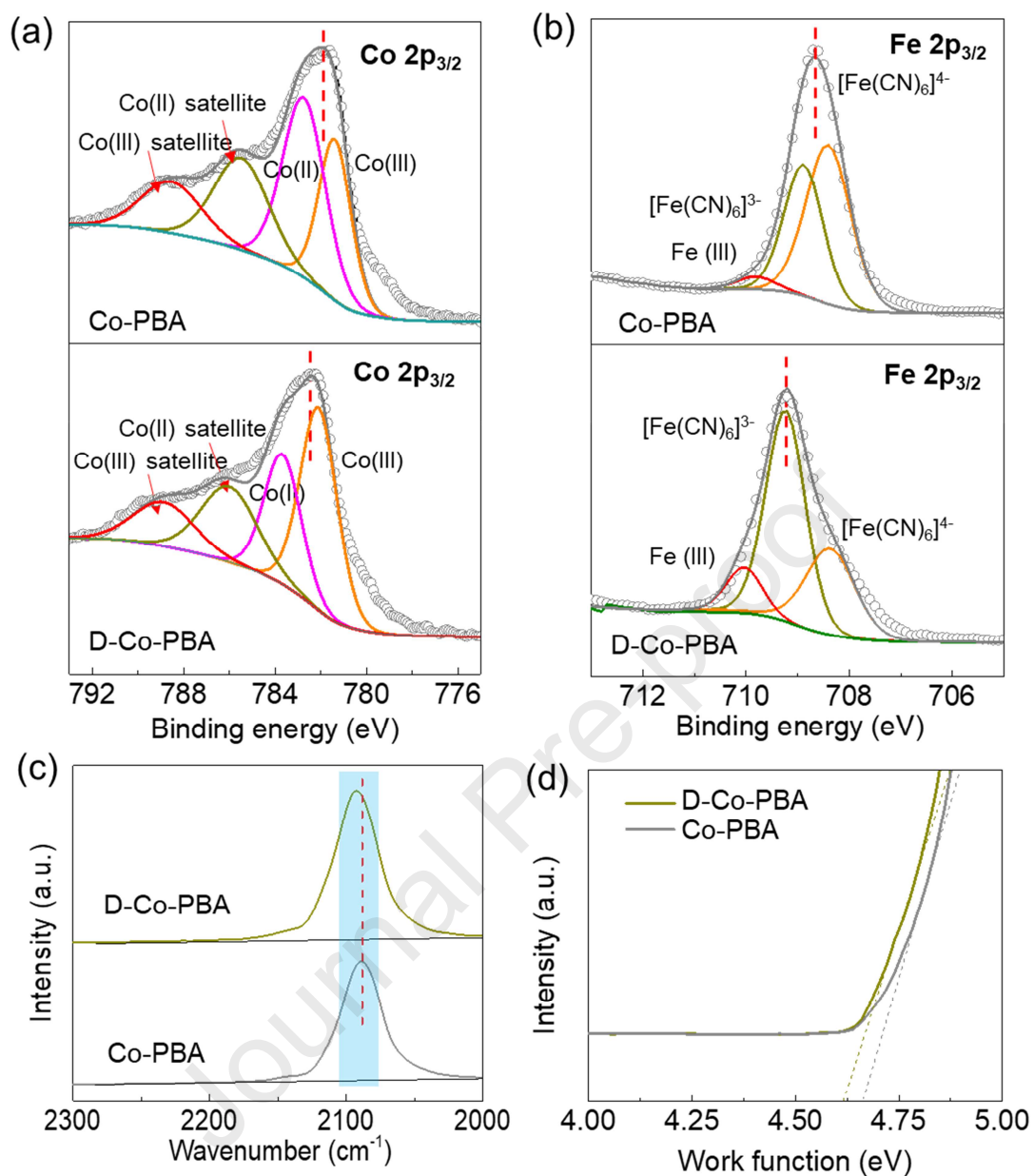
Fig. 3 XPS spectra of Co-PBA and D-Co-PBA. (a) Co 2p. (b) Fe 2p. (c) FTIR spectra

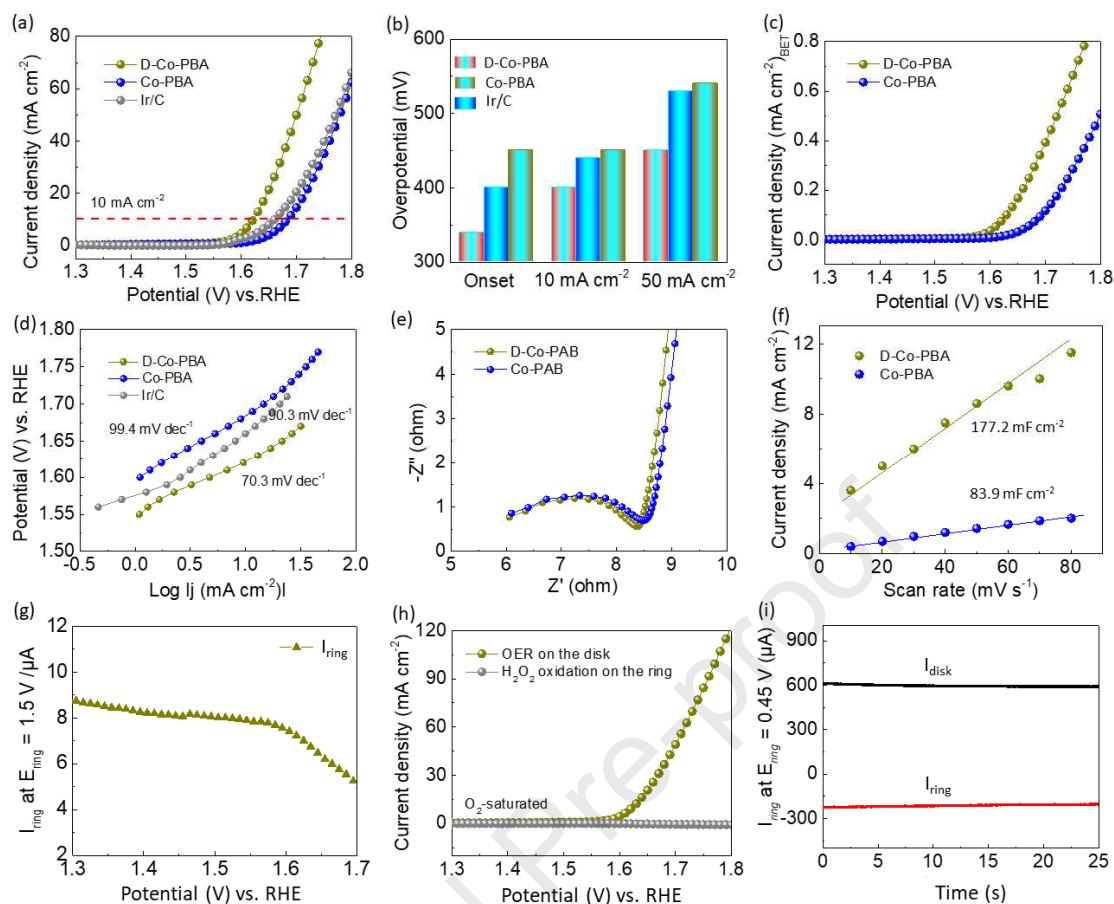of Co-PBA and D-Co-PBA. (d) UPS spectra of Co-PBA and D-Co-PBA.

3

Fig. 4 (a) LSV curves of Co-PBA, D-Co-PBA, and Ir/C with a scan rate of 10 mV s^{-1} in 1 M KOH. (b) Histograms of onset potential and overpotential at current density of 10 mA cm^{-2} and 50 mA cm^{-2} from LSV curves. (c) Normalized LSV curves on Co-PBA and D-Co-PBA by BET surface area. (d) Corresponding Tafel slope plots. (e) Nyquist plots of Co-PBA and D-Co-PBA. (f) Linear relationships between capacitive current and scan rate for Co-PBA and D-Co-PBA. (g) Ring current of D-Co-PBA on RRDE with ring potential of 1.5 V in O$_2$-saturated 1 M KOH. (h) Detection of H$_2$O$_2$ generated using RRDE measurement, and ring current of D-Co-PBA on RRDE with ring potential of 1.5 V in O$_2$-saturated 1 M KOH. (i) Ring current of D-Co-PBA on RRDE in N$_2$-saturated 1 M KOH solution (ring potential: 0.40 V).
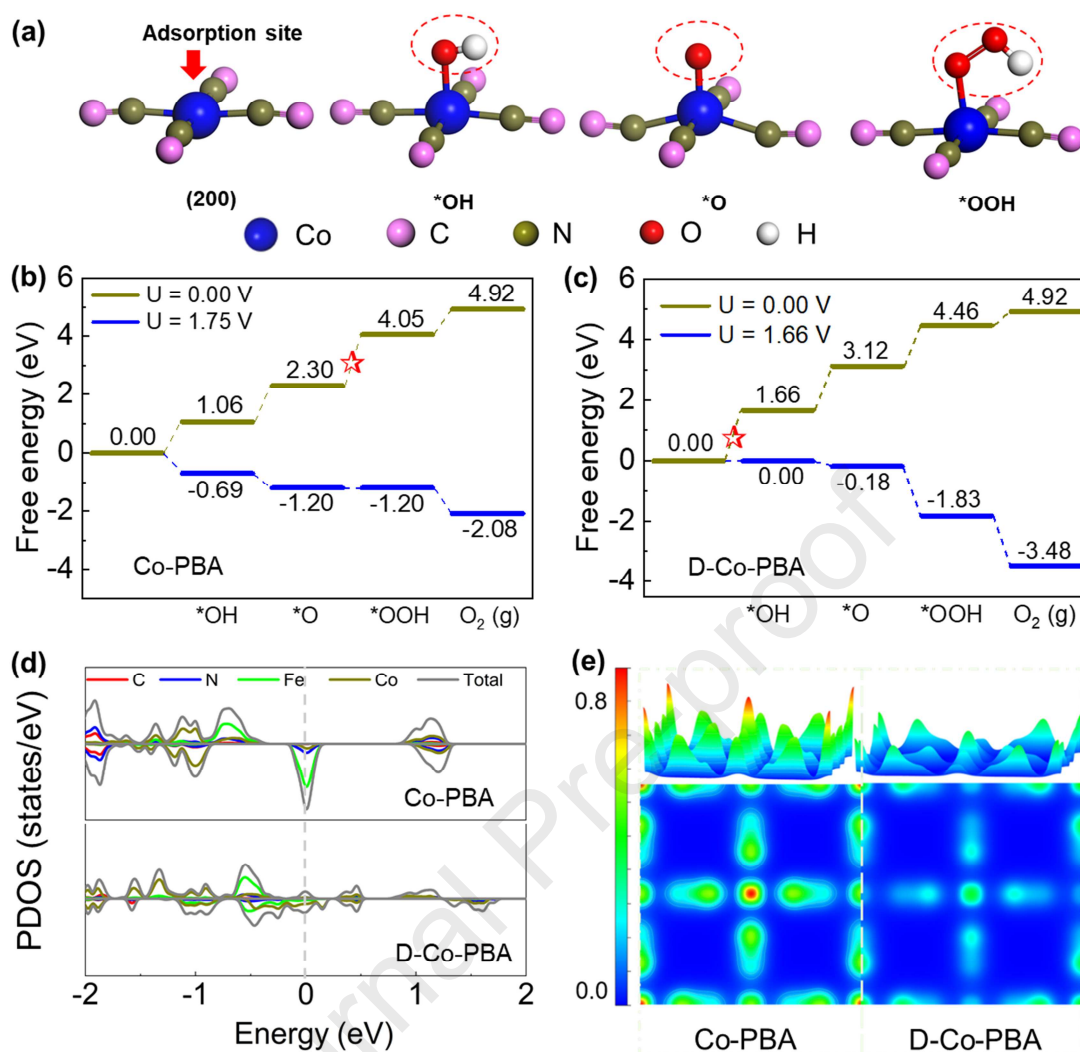
4

Fig. 5 DFT calculation for OER mechanism. (a) Schematic of OER mechanism on D-Co-PBA catalyst in alkaline electrolyte. The pink, yellow, brown, and blue circles represent C, N, and Co atoms, respectively. Free energy diagram for OER on (b) Co-site of Co-PBA and (c) Co-site of D-Co-PBA (star is RDS). (d) Calculated density of states of Co-PBA and D-Co-PBA. (e) Electron density contour maps of Co atom in Co-PBA and D-Co-PBA. The electron density increases as the colour changes from blue to red in the electron density difference plot.
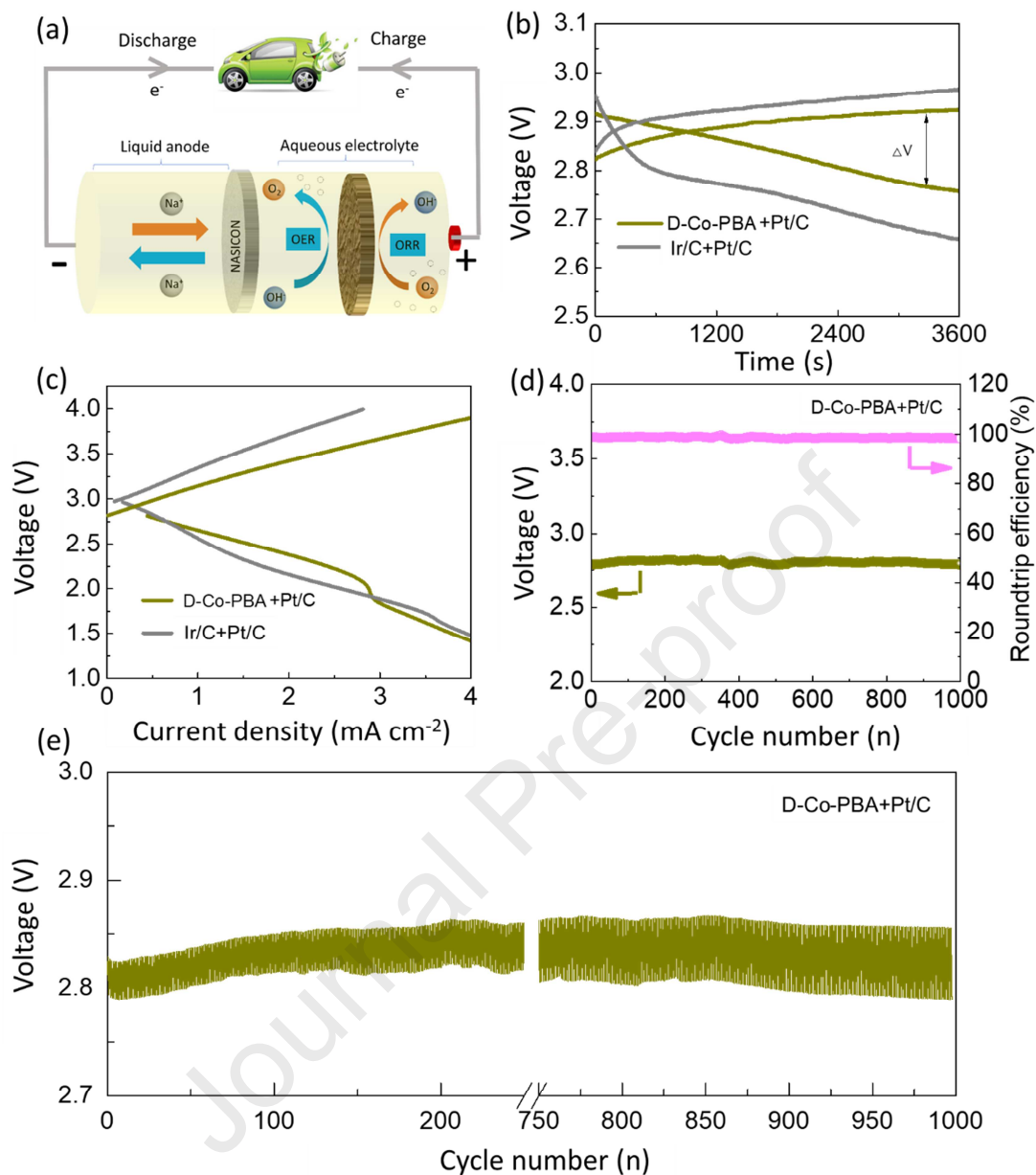
Fig. 6 (a) Schematic of HSAB. (b) Charge–discharge voltage curves of HSABs using different catalysts at current density of 0.01 mA cm^{-2}. (c) Charge–discharge polarization curves of HSABs with different catalysts. (d) Round-trip efficiency and cycling performance of discharge voltage of HSAB using D-Co-PBA + Pt/C catalysts at current density of 0.01 mA cm^{-2}. (e) Galvanostatic cycling of HSAB with D-Co-PBA + Pt/C catalysts at current density of 0.01 mA cm^{-2} (20 min per-charge-discharge).

6

Highlights:

1. We develop a facile high-yield strategy to fabricate defective Co Prussian blue analogue (D-Co-PBA) by breaking bonds of iron carbon-nitrogen-cobalt units, forming abundant $[Fe(CN)_6]$ vacancies.

2. Benefiting from the optimized intrinsic properties and electronic density while exposing Co (III) active sites in PBAs, the catalyst shows a remarkable performance with enhanced kinetics and activity for OER.

3. Density functional theory (DFT) calculations suggest the electronic structure of D-Co-PBA can be tuned by introducing $[Fe(CN)_6]$ vacancy defects, which reduces the reaction barrier of the rate-determining step towards OER, thus improving catalytic performance.

4. A hybrid sodium-air battery assembled with Pt/C and D-Co-PBA catalysts displays a low charging-discharging gap of 0.15 V and high stability up to 1000 cycles. This work demonstrates an excellent promise for large-scale production of cheap defective PBA based materials with desirable OER catalytic activity.

Declaration of interests

☒ The authors declare that they have no known competing financial interests or personal relationships that could have appeared to influence the work reported in this paper.

☐The authors declare the following financial interests/personal relationships which may be considered as potential competing interests: